



UNIVERSITY OF LEEDS

This is a repository copy of *Computational fluid dynamic enabled design optimisation of miniaturised continuous oscillatory baffled reactors in chemical processing*.

White Rose Research Online URL for this paper:  
<http://eprints.whiterose.ac.uk/152860/>

Version: Accepted Version

---

**Article:**

González Niño, C, Kapur, N [orcid.org/0000-0003-1041-8390](https://orcid.org/0000-0003-1041-8390), King, M-F [orcid.org/0000-0001-7010-476X](https://orcid.org/0000-0001-7010-476X) et al. (4 more authors) (2019) Computational fluid dynamic enabled design optimisation of miniaturised continuous oscillatory baffled reactors in chemical processing. *International Journal of Computational Fluid Dynamics*, 33 (6-7). pp. 317-331. ISSN 1061-8562

<https://doi.org/10.1080/10618562.2019.1683169>

---

© 2019 Informa UK Limited, trading as Taylor & Francis Group. This is an author produced version of an article published in *International Journal of Computational Fluid Dynamics* . Uploaded in accordance with the publisher's self-archiving policy.

**Reuse**

Items deposited in White Rose Research Online are protected by copyright, with all rights reserved unless indicated otherwise. They may be downloaded and/or printed for private study, or other acts as permitted by national copyright laws. The publisher or other rights holders may allow further reproduction and re-use of the full text version. This is indicated by the licence information on the White Rose Research Online record for the item.

**Takedown**

If you consider content in White Rose Research Online to be in breach of UK law, please notify us by emailing [eprints@whiterose.ac.uk](mailto:eprints@whiterose.ac.uk) including the URL of the record and the reason for the withdrawal request.



[eprints@whiterose.ac.uk](mailto:eprints@whiterose.ac.uk)  
<https://eprints.whiterose.ac.uk/>

# **Computational Fluid Dynamic Enabled Design Optimisation of Miniaturised Continuous Oscillatory Baffled Reactors in Chemical Processing**

Carlos González Niño <sup>a</sup>, Nikil Kapur <sup>a</sup>, Marco-Felipe King <sup>b</sup>, Gregory de Boer <sup>a</sup>,  
A. John Blacker <sup>c</sup>, Richard Bourne <sup>c</sup> and Harvey Thompson <sup>a</sup>

<sup>a</sup> School of Mechanical Engineering, University of Leeds, LS2 9JT, United Kingdom

<sup>b</sup> School of Civil Engineering, University of Leeds, LS2 9JT, United Kingdom

<sup>c</sup> School of Chemistry and School of Chemical and Process Engineering, University of Leeds,  
LS2 9JT, United Kingdom

# Computational Fluid Dynamic Enabled Design Optimisation of Miniaturised Continuous Oscillatory Baffled Reactors in Chemical Processing

## ABSTRACT

The first CFD-enabled multi-objective design optimisation methodology for continuous oscillatory baffled reactors (COBRs), used for flow chemistry-based process development, is described, where performance is quantified in terms of two metrics: a mixing efficiency index and the variance of the residence time distribution. The effect of cross-validation approaches on the surrogate modelling of these performance metrics is examined in detail and the resultant surrogate models used to demonstrate the influence of key design variables. Pareto fronts of non-dominated solutions are presented to illustrate the available design compromises for COBR performance and it is shown that these can give a narrow Residence Time Distribution and good mixing within the final design. The novel feature of offset baffles within a channel, explored here for the first time, is identified as a key parameter in improving the performance of COBRs.

**Keywords:** Continuous oscillatory baffled reactor; surrogate modelling; multi-objective optimisation; machine learning

## 1. Introduction

The inexorable demand for better reaction yields in chemical production processes has led to increasing reliance on small-scale studies for effective process optimisation<sup>[1-4]</sup>. A range of different small-scale flow chemistry platforms for reaction screening have been developed in recent years in order to determine optimal synthesis routes<sup>[5]</sup> with minimal chemical consumption<sup>[6]</sup> enabling real-time at-line<sup>[7]</sup> and in-line<sup>[8]</sup> analysis. These characteristics make possible the implementation of self-optimising routines for which the reaction outputs can be optimised computationally through computers connected to the laboratory instrumentation.

A number of reactors have been used in this way, including micro-reactors<sup>[9-14]</sup> and tubular reactors<sup>[7, 15, 16]</sup>. The flow regime in micro-reactors is laminar and the mixing mechanism is dominated by diffusion due to the small scales and low flow rates employed<sup>[17]</sup>. Tubular reactors, while operating at higher flow rates and volumes at the scale of millilitres, do not provide good mixing due to low Reynolds numbers and negligible radial velocity components<sup>[18]</sup>.

Continuous oscillatory baffled reactors (COBRs) can overcome these limitations<sup>[4]</sup> to achieve near plug flow under laminar flow conditions, through minimising mixing of fluid

entering the reactor at different times <sup>[19]</sup>, whilst providing good local mixing thereby reducing the formation of by-products. COBRs are formed from a tubular reactor with periodic internal baffles, where the mixing of the species is intensified through the formation of vortices around these. An oscillatory and reversing flow is created using a pump, piston or diaphragm, and it is the combination of this kind of flow and the baffled reactor geometry that enables the generation of vortices which greatly enhances mass and heat transfer <sup>[20,21]</sup>. Figure 1 illustrates the flow behaviour at different phases of the oscillation within a COBR. As the flow accelerates, vortices form and expand downstream of the baffles. During flow deceleration, the vortices continue expanding until the flow reverses and they are forced into the centre of the column to finally unravel into the main stream. Then, the same process is repeated in the opposite direction <sup>[22, 23]</sup>. COBRs use several small volume cells to achieve good mixing in multiphase reactions with near plug flow conditions at low net flow Reynolds numbers <sup>[24]</sup> and have proven effective in a range of important chemical production processes including polymerisation <sup>[25]</sup>, crystallization <sup>[26]</sup>, particle suspension <sup>[27]</sup>, multiphase reaction <sup>[28]</sup> and biofuel production <sup>[24]</sup>.

It has been shown that near plug flow can be induced through sufficiently long cascades of continuous stirred tank reactors (CSTR) –in fact, the residence time distribution (RTD) of a COBR can be mathematically modelled like a CSTR cascade <sup>[29]</sup>. A comparison of the residence time distributions for CSTRs and COBRs for a different number of reactors/cells is given in Figure 2. As the number of cells increases, the RTD curves become narrower around the mean residence time ( $t/t_m=1$ ). Regarding RTD, the use of a high number of small cells COBR largely outperforms common CSTRs cascades, which even in recent miniaturised versions rarely exceed 5 reactors <sup>[30]</sup>.

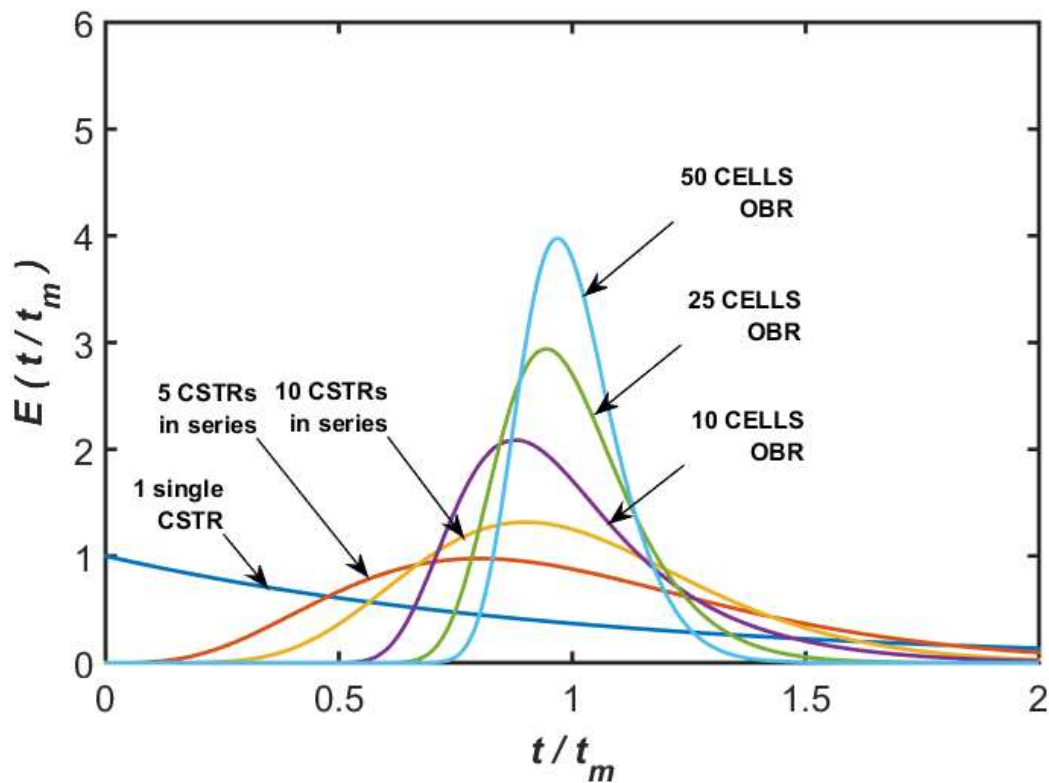


Figure 2. Residence time distributions for CSTRs and OBRs for a different number of cells. CSTR curves represent well mixed CSTRs following [31], while COBR curves for 10, 25 and 50 cells were obtained from CFD simulations in this work.

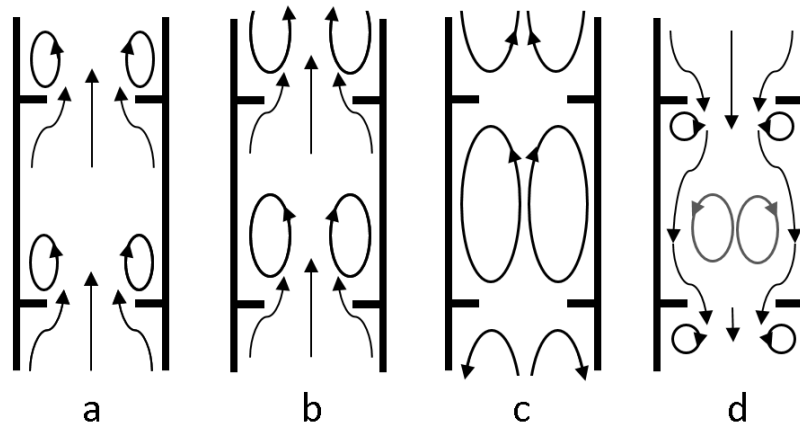


Figure 1. Diagram of the flow in a single stage of a COBR for different oscillation phases. a) Beginning of the upstroke and vortices formation. b) Flow acceleration and vortex expansion. c) Maximum vortex expansion after flow deceleration. d) Flow inversion forcing the vortices into the main flow stream as they fade. New vortices similar to those in a) but in the opposite direction starting to form. Adapted from [22].

Mesoscale oscillatory baffled reactors were first introduced as a laboratory scale reactor by Harvey et al. [32] with the objective of optimising the production of sterols in a saponification reaction. Further work concerning the characterisation of the residence times and mixing in

such reactors under different fluid oscillation frequencies and amplitudes was carried out by Reis <sup>[33]</sup>. Harvey et al. continued the work in mesoscale COBRs by comparing the residence time distribution for different baffle designs <sup>[34]</sup>, quantifying fluid mixing properties <sup>[35]</sup> and the effect of geometrical parameters <sup>[36]</sup> by analysing the RTD and its variation throughout the flow. Their smallest mesoscale reactors had dimension of 4.4 mm outer diameter, 1.6 mm inner diameter and 7.5 mm spacing between adjacent baffles <sup>[35]</sup>. Later studies explored the feasibility of further miniaturisation of COBRs for manufacturing silver nanoparticles with a high degree of control over particle size <sup>[37]</sup>. These represented a 6-fold reduction in cell volume compared to the smallest COBR investigated previously by Harvey et al. Planar OBRs have previously been demonstrated to give good RTD <sup>[38]</sup> where constrictions are formed by smoothly varying channel walls.

Computational fluid dynamics (CFD) is being used increasingly to understand flow fields within COBRs and to determine axial dispersion and shear strain rates. Mannien et al. <sup>[39]</sup> used CFD to evaluate axial dispersion and mixing performance of a COBR, introducing the concept of the velocity ratio  $R_v$  for a unit cell. Mazubert et al. <sup>[40, 41]</sup>, explored the effect of baffle geometry on the velocity ratio, pressure drop, and energy dissipation for five different COBR designs and demonstrated that COBR geometry had a huge impact on the flow behaviour <sup>[40]</sup>. The second part of their study <sup>[41]</sup> introduced novel characterisation techniques, using particle tracking to determine radial and axial fluid stretching, as well as the shear strain rate history. Reis et al. <sup>[42]</sup> proposed using CFD to understand the flow in COBRs through the radial and axial velocities and the vorticity, analysing the number, position and area of the vortex rings, which they assumed to be elliptical. However, methods for formal optimisation of such a problem have not yet been established, providing a strong motivation for this work.

This study proposes the first CFD-enabled design optimisation methodology for COBRs. It develops innovative post-processing techniques to determine the mixing efficiency index and residence time distributions for a range of different COBR geometries and uses the data to carry out the first multi-objective optimisation of COBRs. The planar design of the COBR brings with it the potential for ease of manufacture, with flexibility in material choices, a small operating footprint and scalability. The paper is organised as follows. The problem specification is given in section 2 and the CFD and post-processing methods are described in section 3. The multi-objective optimisation methodology is given in section 4 and a series of illustrative results are presented in section 5. Conclusions are drawn in section 6.

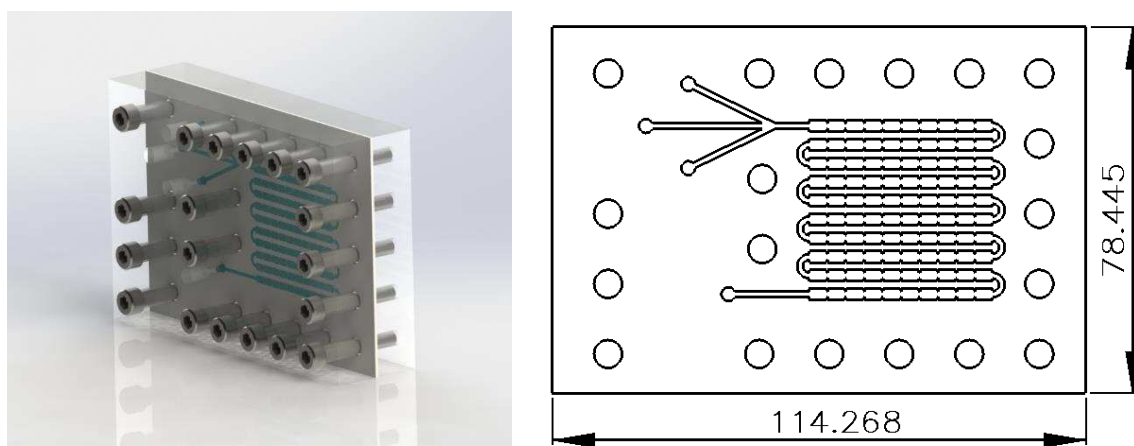


Figure 3. Design of our novel plate mCOBR for chemical self-optimisation and discovery. All units shown in mm.

## 2. Problem Specification

### 2.1 COBR Geometry Specification

The proposed plate mCOBR geometry in this study is shown in Figure 3. Within each channel there is a series of baffles whose geometry is specified in terms of the parameters shown in Figure 4. The relations between different geometry parameters and its effect on mixing and residence time distribution have been explored experimentally for cylindrical COBRs<sup>[43, 44]</sup>. Traditionally, the geometrical parameters studied that govern the performance of the reactor are the baffle spacing  $L$  (often as a ratio of the diameter of the reactor ( $L/D$ )), the free baffle area ( $e/D$ ) and the baffle thickness. Whilst there has been some work on smoothly varying periodic baffles in two-dimensions<sup>[38]</sup>, we limit the design space to discontinuous changes in channel width to minimise the degrees of freedom within the optimisation framework.

When the baffle spacing is small, the vortices formed in each cell reach the next one before fully developing, thus reducing radial dispersion and deviating from plug-flow behaviour. For large baffle spacing, stagnant zones will form in each cell as a result of the vortex only extending partway through the cell. The baffle open area is also very influential. If it is too big then the small baffles generate narrow vortices, leading to poor mixing. Such configurations also lead to a high degree of channelling, deviating from plug flow. Contrarily, when the baffle open area is too small, the vortices generated do not expand through the entirety of the cell, resulting in stagnant zones that have an adverse effect on both mixing and residence time distribution. For most practical applications the ratio baffle open area lies between 0.2 and 0.3<sup>[43]</sup>. The results of studies on the effect of baffle thickness indicate that thinner baffles promote the generation of vortices<sup>[44]</sup>.

The COBR geometries considered here are formed by combining identical two-dimensional cells with the parameters shown in Figure 4. A 2D approach was undertaken, as the outcome of 2D CFD simulations for channels of varying geometry are generally regarded

as a good representation of 3D models unless there are complex 3D flow structures driven by the geometry <sup>[45]</sup>. Three design variables are considered: the length to width ratio ( $L/D$ ), the ratio of the open space between baffles and the cell width ( $e/D$ ) and the ratio of the offset distance between the baffles,  $a$ , to the total cell length,  $L$ ,  $a/L$ . The effect of the latter parameter on COBRs has not been considered previously. In all cases considered throughout the study, the unit cell area will be  $8.75 \text{ mm}^2$  for this plate mCOBR. This was chosen to give a reactor volume of  $1.75 \text{ mL}$  (similar to other meso-scale reactors) based on a manufacturable design with 100 cells cut into a plate of thickness  $2 \text{ mm}$ .

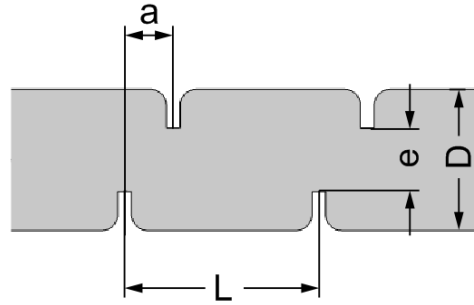


Figure 4. COBR Cell Geometry Parameters.  $L$  is the distance between two adjacent baffles,  $D$  is the width of the cell,  $e$  is the open space between the baffles and  $a$  is the offset between baffles.

### 3. CFD Modelling

Two-dimensional, laminar flow within a COBR is governed by the incompressible Navier-Stokes and continuity equations:

$$\frac{\partial \mathbf{u}}{\partial t} + (\mathbf{u} \cdot \nabla) \mathbf{u} = -\nabla \cdot \left( \frac{p}{\rho} \right) + \nu \nabla^2 \mathbf{u} \quad (1)$$

$$\nabla \cdot \mathbf{u} = 0 \quad \nu = \frac{\mu}{\rho} \quad (2)$$

At the inlet, the following time-dependent velocity profile for the average inlet velocity as a sinusoidal function of time is specified with a frequency of  $5 \text{ Hz}$  and a period of  $2 \text{ seconds}$ , defined so that the residence time in a hundred cells long reactor is approximately one minute, a typical time-scale of chemical reactions:

$$u_{av}(t) = 61.7 \cdot (0.25 + \sin(10\pi t)) / e \text{ [mm/s]} \quad (3)$$

The inlet velocity has both positive and negative values and is defined to ensure that the flow rate and thus the mean residence time for all the geometries is the same regardless of their inlet width,  $e$ . A representation of the inlet flow rate can be found in the supporting documentation (Figure S1). The phase of the oscillation  $\phi(t) = 10\pi t$  will be taken into account to compare the fluid flow at different moments during an oscillation.

A no slip boundary condition is imposed for the stationary walls of the reactor, and at the outlet boundary the pressure is set to 0 Pa. All the properties of the fluid are set to be those of water at 293.15 K, with  $\mu = 0.0010 \text{ Pa}\cdot\text{s}$  and  $\rho = 1000 \text{ kg/m}^3$ .

After the flow field is determined, the transport of a dilute chemical species through advection and diffusion is used to characterise the mixing and residence time. This is governed by the following equation:

$$\frac{\partial c}{\partial t} = \nabla \cdot (D\nabla c) - \nabla \cdot (uc) \quad (4)$$

where the diffusion coefficient  $D$  was set to  $10^{-9} \text{ m}^2/\text{s}$ , representative of a typical small molecule in an aqueous solvent <sup>[46]</sup>.

At the walls of the reactor a condition of no flux of diluted species is imposed,

$$n \cdot (-D\nabla c) = 0 \quad (5)$$

and at the outflow boundary the diluted species is transported by advection only.

### 3.1. Spatial and Temporal Periodicity

The COBR studied here consists of 16 cells as shown in Figure 5 (e). This is chosen as a geometry under which a periodic flow across a number of cells is established within the middle section of these 16 cells, i.e. cells not influenced by the inlet or outlet boundary conditions. Optimising the flow within this section will then provide the design of a cell which can be repeated within a longer geometry to give a reactor of a pre-determined volume.

A key issue to analysing the performance is to be able to determine when spatial and temporal periodicity is achieved within the COBR. As a first approximation a steady flow with a constant inlet velocity, set to the maximum positive inlet velocity, is analysed in order to indicate where inlet boundary effects can be neglected. A grid independence test was carried out evaluating the velocity magnitude in the central point of the cell. The study was computed for five different meshes using the finite element software Comsol Multiphysics (Comsol Inc., USA), with between 1264 and 11,484 elements per cell. It was ascertained that a mesh of 5276 elements produced a mesh-independent solution, as presented in Figure 5 (a). Consequently, meshes of this size were employed across all geometries examined in the present study. A histogram for vertex skewness is presented in Figure 5 (b). The mean skewness is 0.1853. It

can be seen that the vast majority of elements have a skewness less than 0.4, indicative of a high-quality mesh. A typical mesh of 5000 elements used in this study is shown in Figure 5 (c).

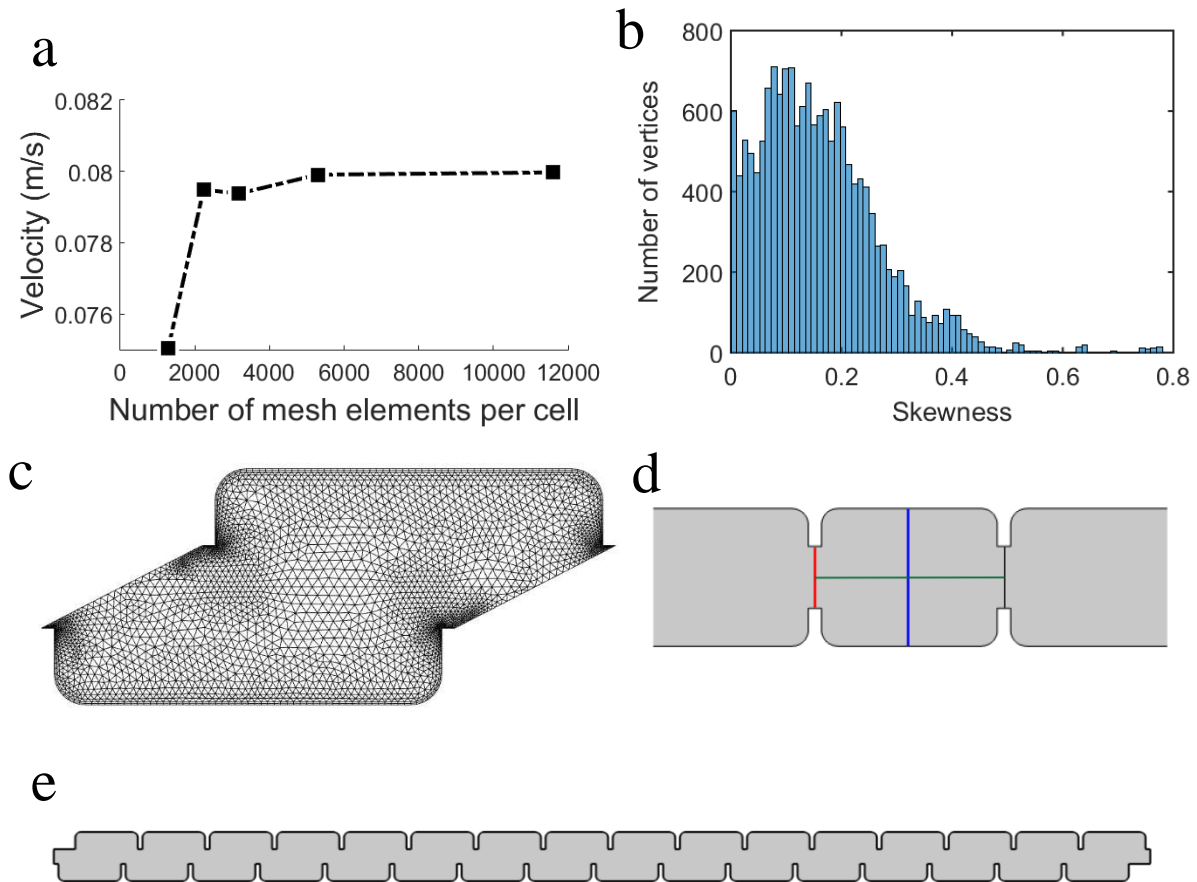


Figure 5 a) Velocity at the middle point of the geometry for a variety of different mesh sizes. b) Histogram showing element skewness. c) Mesh with 5816 elements per cell as used in this study. d) Cut lines on which solutions are obtained. e) Example of a full 16 cells long computational domain.

Fluid velocities on the green longitudinal cut lines shown in Figure 5 (c), for cells one to four (counted from the inlet) are given in Figure 6. They show that the maximum percentage error in velocity between cells 3 and 4 is less than 0.125%. On this basis, it is taken that the

inlet boundary effects are negligible from cell 3 onwards and hence spatial periodicity is reached from this point.

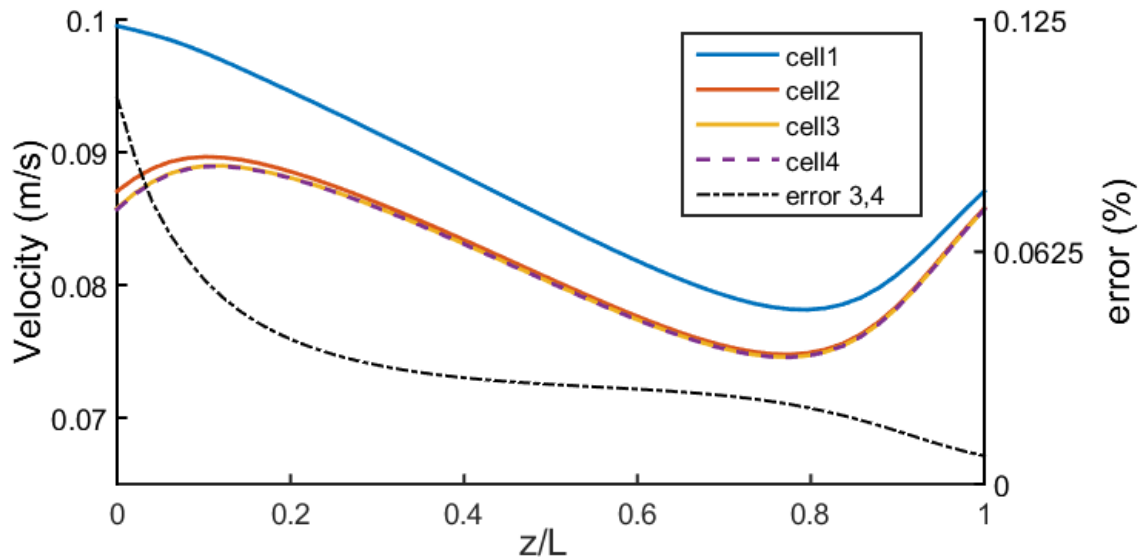


Figure 6 Longitudinal velocities on the green cut line for the first four COBR cells.

Temporal periodicity is considered next using the mesh optimised for the steady-state simulation. The transverse velocity profiles along the centre line (blue cut line in Figure 5 (d)) were determined for a time-dependent simulation over 1 second, corresponding to five complete periods. Figure 7 shows the differences between the velocity profiles of cycles 4 and 5 for the third cell in the reactor. The discrepancy amongst the 4<sup>th</sup> and 5<sup>th</sup> time period was typically less than 0.3%.

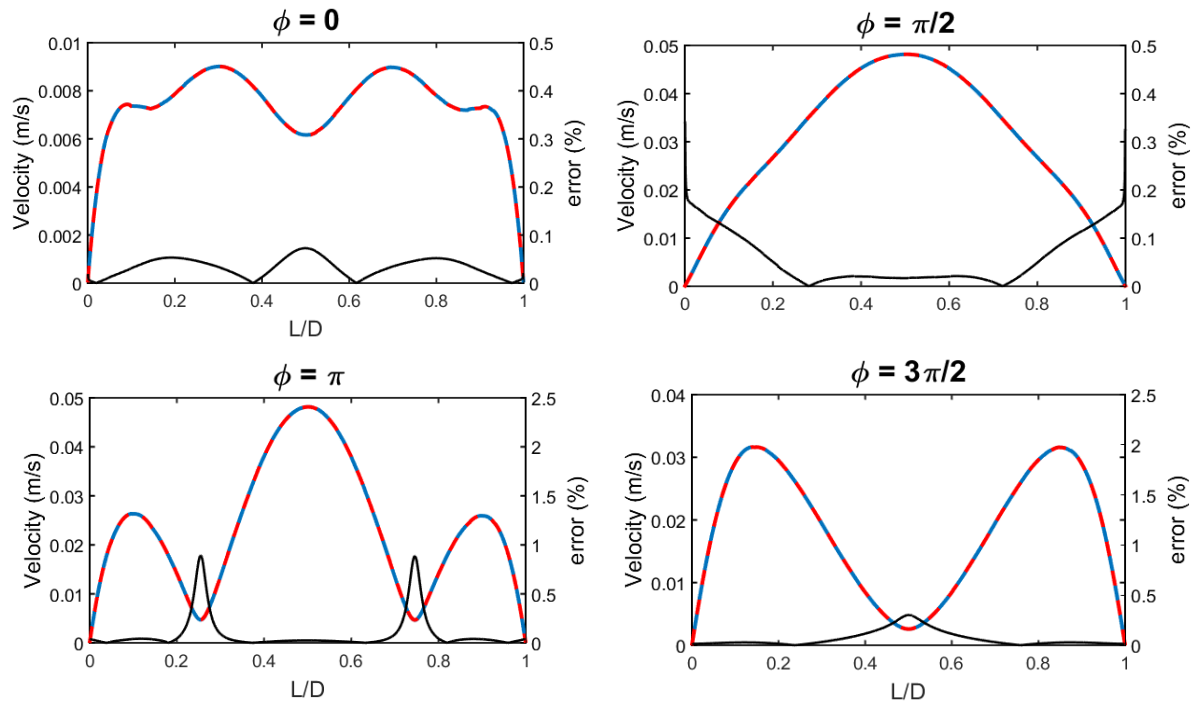


Figure 7. Transverse velocity profiles and the discrepancy between cycles 4 and 5 for cell 3 for different oscillation phases.

Spatial periodicity was again considered for the time-dependent scenario to verify the conclusions from the preliminary analysis. A comparison of the different velocity profiles along the three cut lines defined in Figure 5 (d) for cells 3 and 4 revealed that the discrepancy was significantly below 2% at any time of the fifth cycle, indicating spatial periodicity of the time-dependent solution from cell 4 onwards. Table 1 presents the values of the maximum relative error between the velocity profiles for different oscillation phases. Based on these findings, CFD solutions were computed for five cycles. The periodic time-dependent flow from the fifth cycle (lasting 0.2s) was then taken in isolation and used to construct a new time dependent flow field of 100 periods in length (representing 20s), thus giving a representative flow field without incurring additional computational cost.

Table 1 Maximum relative error between cells 3 and 4 at different oscillation phases and cutlines.

$\phi$	0	$\pi/4$	$\pi/2$	$3\pi/4$	$\pi$	$5\pi/2$	$3\pi/2$	$7\pi/2$
<b>Blue</b>	0.65	0.42	0.25	0.64	0.70	0.60	0.57	0.59
<b>Red</b>	0.49	0.35	0.55	0.40	0.31	0.45	0.37	0.60
<b>Green</b>	0.61	0.28	0.27	0.48	0.65	1.20	0.38	0.57

To ensure confidence in the numerical scheme, validation was carried out by comparing a CFD model (Figure S2) to the experimental data taken from Armaly<sup>[47]</sup> for a backward facing step under laminar conditions. This was chosen as the flow features within this problem are

similar to those found within the COBR. The mesh elements for the validation was chosen to give a similar density between the two simulations. Consequently 1237 mesh elements were used for the backward facing step which is geometrically similar to a quarter of a COBR cell (see supporting documentation for more information). The CFD model was shown to be converged and that there was good agreement between these predictions and the experimental data in terms of the re-attachment length for Reynolds numbers up to 500 (Figure 8) and velocity profiles at different lengths from the step and under different Reynolds numbers (Figures S3 and S4 in supporting documentation). The Reynolds number as defined in Armaly was under 200 for all COBR simulations considered. Due to the similarity of the flow features and operating conditions, this gives confidence in the ability to capture the behaviour of the COBR using CFD.

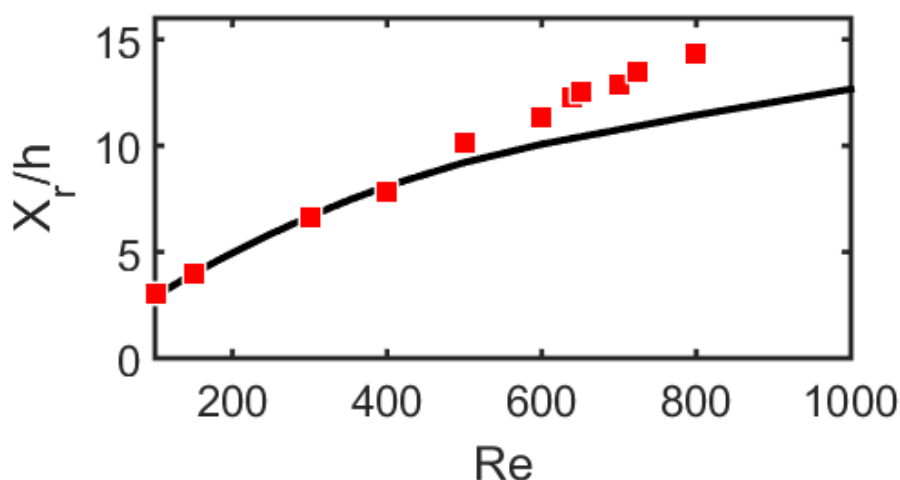


Figure 8. Re-attachment length normalised by the step size under different Reynolds numbers. Black line: CFD simulation. Red squares: *Armaly's experimental data* <sup>[47]</sup>.

## 3.2. Post-processing of CFD results

### 3.2.1 Mixing Efficiency Index

The CFD solutions are used to provide information on how effectively a reactor mixes the chemical species and to determine the residence time distribution in the flow. A range of methods have been used to assess the mixing capabilities of different reactor geometries with, perhaps, the simplest being to calculate the standard deviation of the concentration or of some associated property, such as the pixel intensity in experimental studies in a cross-section of the reactor <sup>[48-50]</sup>. The corresponding dimensionless quantity, where the standard deviation is divided by the mean concentration, is referred to as the absolute mixing index <sup>[51]</sup>. A related approach is the use of a relative mixing index (RMI) which compares the standard deviation of the concentration in a cross-section with the standard deviation of the unmixed state as depicted in Figure 9 (top) at time 0 <sup>[52, 53]</sup>. Other approaches include the use of particle tracking to determine mixing efficiency by calculating radial and axial fluid stretching <sup>[41]</sup>, albeit at high computational cost. The relative mixing index is used in this study and defined as

$$\eta = \left[ 1 - \left( \frac{\sqrt{\frac{1}{N} \sum_1^N (C_i - C_{p,i})^2}}{\sqrt{\frac{1}{N} \sum_1^N (C_{p,i} - C_{0,i})^2}} \right) \right] \quad (6)$$

where  $C_i$  represents the concentration of the species at the location  $i$  for the case being evaluated, and  $C_{p,i}$  and  $C_{0,i}$  are the concentrations of the perfectly mixed case and of the totally unmixed state, respectively, at the same location  $i$ .

With an oscillating flow and complex shape of the cells the relative mixing index  $\eta$  varies with both time and position of the cross-section in the cell. A new strategy was therefore developed here to assess the mixing efficiency in a time dependent flow field. At initialisation, the reactor is split in half as shown in Figure 9 with the bottom half of the reactor set to a concentration of  $100 \text{ mol/m}^3$  while the upper half is set to a concentration of  $0 \text{ mol/m}^3$ . Then the species is allowed to transport according to equation (4) using the flow field assembled from a single representative period as described in section (3.1).

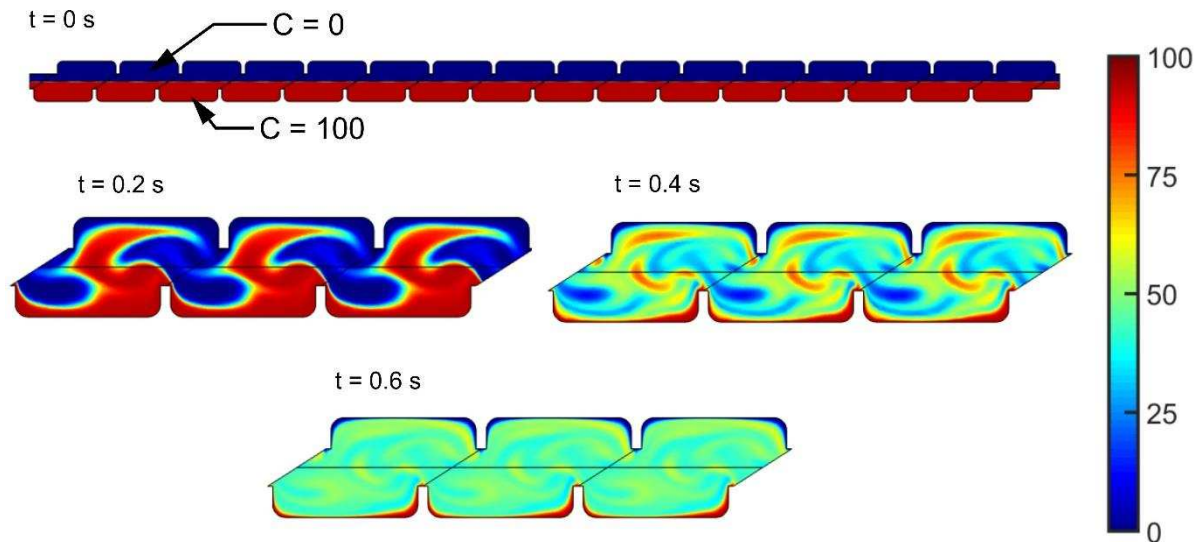


Figure 9. Initial state of the reactor (top figure) and state of three adjacent cells for three different times. The geometry parameters in this case are:  $L/D=1.5$ ,  $e/D=0.5$  and  $a/L=0.25$ . Colour: concentration [ $\text{mol/m}^3$ ]

The degree of mixing is then calculated within the 13<sup>th</sup> cell from the inlet by evaluating  $\eta$  on a grid of  $50 \times 25$  evenly-spaced points, covering the whole area of the cell, at 8 separate time points within a cycle. This cell was selected to avoid inlet and outlet effects. Figure 10 shows calculated  $\eta$  values for 4 different reactor designs. The mixing performance is captured at the 6<sup>th</sup> time period since this shows good sensitivity between different designs.

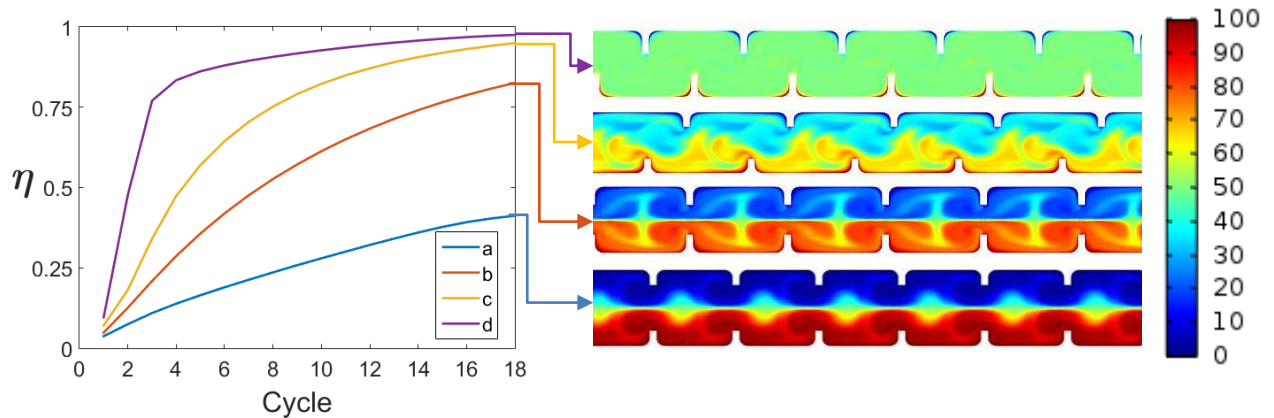


Figure 10. Temporal evolution of the mixing efficiency index for different geometries (left) and representations of the concentrations in the reactors for the last timestamp of the 6<sup>th</sup> cycle (right). The geometries, from top to bottom, correspond to values of  $L/D$ ,  $e/D$  and  $a/L$  of (1.375, 0.3, 0.5), (1.75, 0.6, 0.25), (1.5, 0.45, 0) and (1, 0.6, 0), respectively.

### 3.2.2 Residence Time Distribution (RTD)

Following previous CFD studies for COBRs [39], RTD is determined using a tracer approach [19, 31]. Initially, the concentration is set to 100 mol/m<sup>3</sup> at the vertical cut line in the 4<sup>th</sup> cell shown in Figure 11 ( $t=0$  s), with the concentration in the rest of the reactor set to zero. The average concentration 10 cells downstream of this point is then plotted as a function of time.

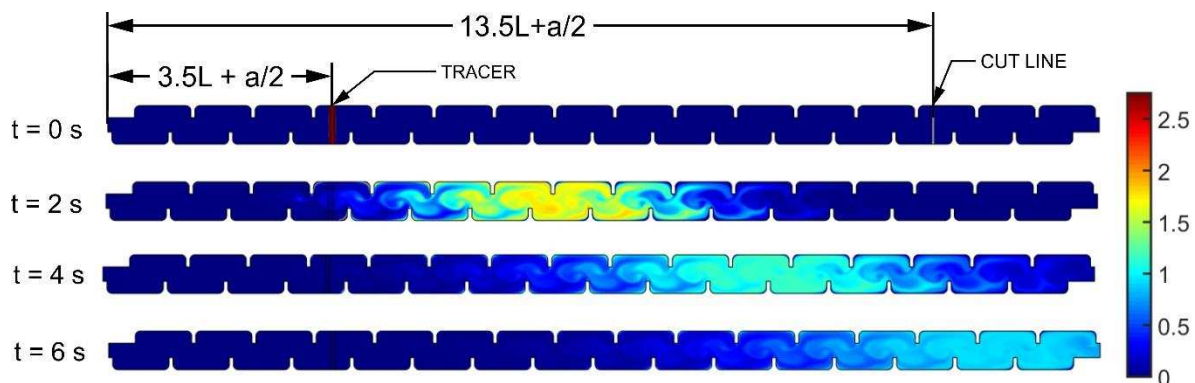


Figure 11. Concentrations at different times (0, 2, 3 and 6 seconds) for the tracer study. The geometry corresponds to values of  $L/D=1.5$ ,  $e/D=0.3$  and  $a/L=0.25$ .

An example of a concentration curve is shown in Figure 12. Due to the oscillatory nature of the flow, the curve has a series of peaks and valleys superimposed onto some overall response. Splitting the data into different oscillation phases results in smooth curves without this perturbation; concentration curves for cycle phases  $3\pi/4$  and  $7\pi/4$  are shown in Figure 12. All concentration values lie between these phases for the case illustrated and the curve has the bell shape similar to that reported for tanks-in-series [19, 31].

The concentration curves for 8 different phases within a time period were calculated and the RTD determined from a velocity weighted average of this data. The RTD function,  $E(t)$ , is obtained by dividing the resulting concentration curve by the area under it.

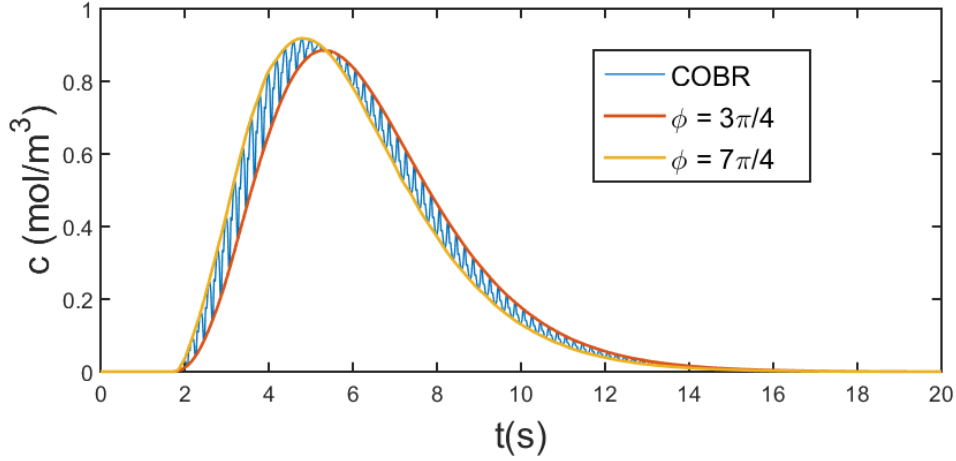


Figure 12. Concentration curve of a COBR obtained from a pulse input simulation for the geometry  $L/D=1.375$ ,  $e/D=0.45$  and  $a/L=0$ .

The dispersion of an RTD can be quantified by its variance <sup>[31]</sup> with small variances indicating a narrow RTD. This is defined by

$$\sigma^2 = \int_0^{\infty} (t - t_m)^2 E(t) dt \quad (7)$$

Within this framework, it is now possible to design a reactor with a narrow RTD which ensures fluid elements entering the reactor spend very similar times within it, minimising the presence of un-reacted materials and unwanted by-products in the reactor's output.

#### 4. Optimisation Methodology

This section explores how COBR design can be optimised to maximise the mixing efficiency  $\eta$  and minimise the variance  $\sigma^2$  of the RTD. The methodology will be demonstrated on the multi-objective optimisation problem defined in (8):

$$\begin{aligned} \text{minimise: } & \frac{1}{\eta} \left( \frac{L}{D}, \frac{e}{D}, \frac{a}{L} \right), \quad \sigma^2 \left( \frac{L}{D}, \frac{e}{D}, \frac{a}{L} \right) \\ \text{subject to: } & 1 < \frac{L}{D} < 1.75, \quad 0.3 < \frac{e}{D} < 0.6, \quad 0 < \frac{a}{L} < 0.5 \end{aligned} \quad (8)$$

##### 4.1 Machine Learning-Enabled Surrogate Modelling

The recent review by Haftka et al. <sup>[54]</sup> noted that for multi-objective problems with less than 100 design variables an effective approach is to use a gradient-free method where surrogate models of the system responses are used to create Pareto fronts which quantify the available compromises between competing objectives. In a first approximation a  $3^3$  full factorial Design of Experiments (DoE) with  $n=27$  points along with a  $2^3$  nested holdout dataset are used to generate the CFD data for surrogate models of  $\eta$  and  $\sigma^2$  throughout the design space. The latter are created using the Moving Least Squares (MLS) method, a generalisation of the least squares

method where weights are functions of the Euclidean distance between the DoE points and the point at which the surrogate model is being created <sup>[55]</sup>. A Gaussian weight decay function is used to determine the weighting of points in the regression analysis at each design point  $\underline{x}$  <sup>[56]</sup>:

$$w_i(\underline{x}) = \exp(-\theta \|\underline{x} - \underline{x}_i\|^2)$$

where  $\|\underline{x} - \underline{x}_i\|^2$  is the Euclidean distance between the design point  $\underline{x}$  at which the surrogate is being calculated and the  $i$ th DoE point  $\underline{x}_i$ , and  $\theta$  is a closeness of fit parameter which provides a means of tuning the surrogate model. In the current study, the design variables are normalised into the unit cube to avoid scaling issues and a second-order polynomial base is used for MLS. Optimal values of  $\theta$  are determined using the Leave One Out cross-validation (LOOCV) <sup>[56]</sup> and Monte Carlo cross-validation (MCCV) <sup>[57]</sup> techniques widely used within Machine Learning to remove biases within predictions <sup>[58]</sup>, combined with a golden search algorithm to minimise the computed root mean square error (RMSE).

LOOCV removes one point from the DoE data set and uses the rest of the DoE points to construct the surrogate model and calculate the error at the removed point. This procedure is repeated for every point in the DoE and the root mean squared error (RMSE) computed. MCCV <sup>[59]</sup> is similar to LOOCV but instead removes a random group of  $k$  points to be used as a validation data set while the remaining DoE points are used to create the surrogate model. A random sub-sampling routine was used to select 2000 different groups of  $k$  points to be left out, whilst ensuring that each DoE point has been removed the same number of times. The RMSE is calculated for the group of points left out for every iteration, using a golden search algorithm to find the value of  $\theta$  that minimises the mean of the RMSE over the 2000 iterations. In this way,  $\theta$  is found for LOO and MCCV for different numbers of points left out (3, 5, 7 and 9). The results of the cross-validation procedures are summarised in the supporting documentation (Table S1).

## 4.2. Multi-Objective optimisation

The multi-objective optimisation problem (8) is solved using Matlab to generate the first Pareto front of non-dominated solutions from the surrogate models obtained in the previous section. To refine the search for the Pareto front, new surrogate models were computed carrying out MCCV over the 35 points resulting from the combination of the 27 points of the full factorial and 8 points of the nested hold out dataset with up to 11 DoE points left out. In order to provide a new holdout dataset for further validation of the surrogate models, results were gathered for five points chosen along the first Pareto front (marked as black stars in Figure S6). Cross-validation results are shown in Table 2, where CV RMSE is the minimum average RMSE found by the golden search, Training RMSE represents the RMSE calculated over all 35 DoE points using the surrogate model and Test RMSE refers to the RMSE calculated over the holdout dataset.

Table 2 Cross-validation results. Sample size: 35 points.

	<b>K left out</b>	$\theta$	<b>CV RMSE</b>	<b>Training RMSE</b>	<b>CV <math>\sigma^2</math></b>	<b>Pareto front RMSE</b>
<b><math>\eta</math></b>	1 (LOO)	8.03	0.0575	0.0073	$33.700 \times 10^{-4}$	0.0141
	3	3.58	0.0562	0.0244	$11.751 \times 10^{-4}$	0.0321
	5	2.58	0.0548	0.0290	$7.081 \times 10^{-4}$	0.0359
	7	1.30	0.0561	0.0359	$5.510 \times 10^{-4}$	0.0396
	9	0.82	0.0569	0.0390	$4.997 \times 10^{-4}$	0.0407
	11	0.70	0.0588	0.0399	$4.975 \times 10^{-4}$	0.0410
<b><math>\sigma^2</math></b>	1 (LOO)	3.56	0.0243	0.0084	$6.085 \times 10^{-4}$	0.0081
	3	3.41	0.0226	0.0087	$1.991 \times 10^{-4}$	0.0081
	5	3.12	0.0234	0.0094	$1.348 \times 10^{-4}$	0.0080
	7	3.01	0.0237	0.0097	$1.061 \times 10^{-4}$	0.0080
	9	2.75	0.0255	0.0103	$1.095 \times 10^{-4}$	0.0079

Following <sup>[60]</sup>, the updated surrogate model for  $\eta$  is obtained by using the  $\theta$  value from cross-validation with 11 points removed, where training and test set errors are similar, whereas for the  $\sigma^2$  model, LOO is used as this provides an appropriate balance between the training and test errors, in addition to represent the lowest value for the training error across all the cross-validation procedures. Figure 13 provides a visualisation of these updated surrogate models using isosurfaces.

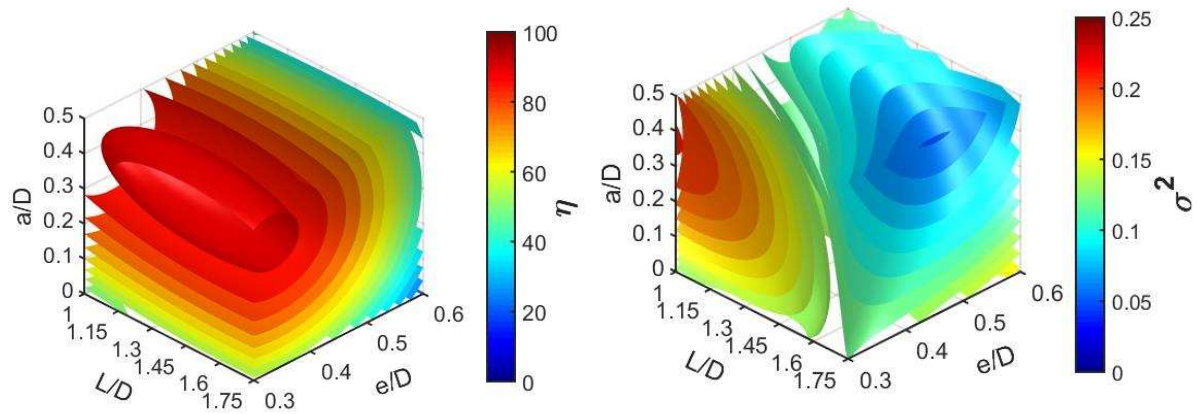


Figure 13. Isosurfaces representations of the models for  $\eta$  (left) and  $\sigma^2$  (right).

For  $\eta$ , the region of interest comprising values higher than 0.9 is in an elongated ellipsoid in the  $L/D$  direction and the  $L/D$  parameter is the least influential design variable. There is clearly a maximum corresponding to  $L/D \approx 1.45$   $e/D \approx 0.34$  and  $a/L \approx 0.38$ . More generally  $e/D$  and  $a/L$  have a significant influence on  $\eta$ . The surrogate model for  $\sigma^2$  is more complex. Its lowest values are obtained for the maximum values of  $a/L$  and  $L/D$  and  $e/D \approx 0.45$ .

This means that an elongated shape of the cell, as well as offsetting the baffles to the maximum, contributes to minimising axial dispersion.

An updated Pareto front, using the updated surrogate models for  $\eta$  and  $\sigma^2$  which use CFD data from the nested hold out DoE in addition to the 27 points full factorial, is presented in Figure 14.

Table 3 Final solution

$x_i$			$f_i$		$f(x_i)$		Absolute error		Relative error (%)	
L/D	e/D	a/L	$\eta$	$\sigma^2$	$\eta$	$\sigma^2$	$\eta$	$\sigma^2$	$\eta$	$\sigma^2$
<b>1.452</b>	<b>0.338</b>	<b>0.379</b>	0.872	0.13	0.927	0.136	0.0605	0.0065	6.98	5
<b>1.749</b>	<b>0.350</b>	<b>0.389</b>	0.867	0.081	0.912	0.076	0.0402	0.0054	4.61	6.61
<b>1.750</b>	<b>0.450</b>	<b>0.500</b>	0.741	0.057	0.774	0.049	0.0334	0.0084	4.51	14.6

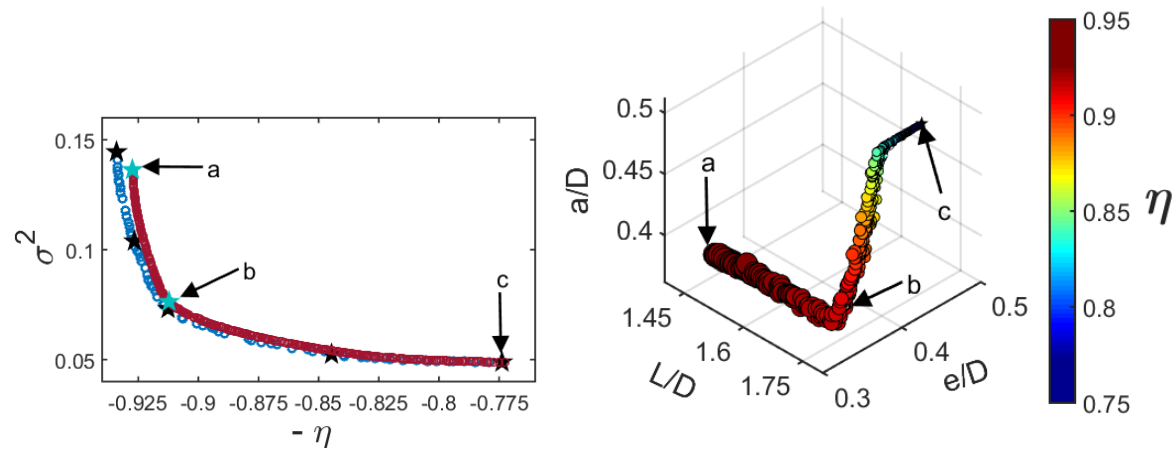


Figure 14. Previous (blue) and revised (deep red) Pareto fronts (left) and representation of the latter in the design space (right), for which *the area of the circles is proportional to  $\sigma^2$* .

When the surrogate models are updated with more CFD data points, the main difference is that the new Pareto front predicts lower values for the mixing efficiency index,  $\eta$ . To assess the accuracy of the updated Pareto front, three points were selected along it. The first point was kept the same as the point selected for a minimum  $\sigma^2$  in the previous front (marked as c in Figure 14) while the other two, shown as cyan blue stars in Figure 14, correspond to the position of maximum curvature of the front and the point on the front predicting the highest  $\eta$  value.

Table 3 presents the results for these points. The geometry configuration calculated as to maximise the curvature of the front, yields values of 0.8721 for  $\eta$ , and 0.0817 for  $\sigma^2$ , hence providing a good trade-off between mixing efficiency and RTD. In this case, the relative errors between the predicted results and the simulation results were of 4.6 and 6.6%, respectively. The highest error of 14.6%, obtained for the minimum  $\sigma^2$  location, suggests the need for a bigger initial DoE or of an iterative approach generating new DoEs in the Pareto Optimality region of the design space. More precise models in this region can be computed, minimising the error over the hold out dataset (points for the previous Pareto front), but in order to establish a reliable Pareto front, the shape of the metamodels needs to be globally correct and not just accurate in a particular region of the design space, even if that region is where the optimum

could be. More generally, the effective use of such cross-validation techniques to achieve an appropriate balance between training and test datasets, is an important means by which machine learning methods avoid biases and improve reliability of predictions.

## 5. Effect of Baffle Offsetting

The flow for the geometry which produces the highest  $\eta$  value is shown in Figure 15 at 6 different phases within a cycle. The flow dynamics differ significantly from the classic symmetric case shown in Figure 1 as a result of baffle offsetting. When the upstroke begins, the fluid accelerates and vortex formation starts on the downstream sides of the baffles. Unlike the case in which there is no offset between the baffles, one of the vortices becomes dominant as a result of the angle that the bulk flow forms with respect to the reactor's longitudinal axis when entering the cell, as shown in Figure 15(a). This dominant vortex occupies almost 75% of the volume of the cell as the flow begins to decelerate, creating a strong recirculation, while the other vortex spreads slightly between adjacent cells (Figure 15(b)). When flow inversion is initiated in the downstroke, the flow separates this dominant vortex from the wall pushing it towards the opposite side of the cell (Figure 15(c)). As this vortex is pushed into the centre of the cell the reversed flow is forced to meander between the two vortices generated in the upstroke until eventually the minor vortex unravels into the main bulk flow (Figure 15(d)). In this fashion, the dominant vortex has been formed and grown in one side of the reactor and then displaced towards the opposite side of the reactor. After the down stroke achieves its maximum velocity and starts to decelerate, two vortices are formed at the upstream side of the baffles. The lower vortex (shown in Figure 15(e)) grows to create the dominant recirculation occupying the length of the cell; this is largely a mirror image of the vortex formation during the upstroke although slightly reduced in strength due to overall net flow through the reactor. The degree of offsetting has an influence in the formation of this vortex. If  $a/L$  is small, the dominant vortex is stronger than the vortex just generated by the backwards bulk flow upstream of the baffle. As  $a/L$  grows, the new vortex becomes stronger than the previous one. This determines the position of the centre of the new vortex, as they spin in the same direction and the weaker one disappears. As depicted in Figure 15(f), as the backstroke continues decelerating, these vortices expand and occupy completely the area of the cell.

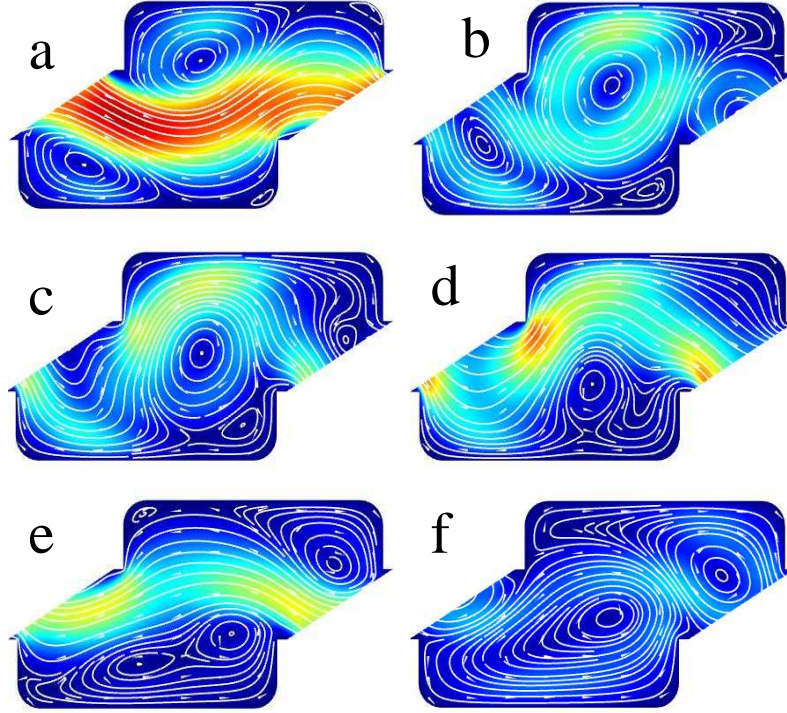


Figure 15. Velocity magnitude colour map, streamlines and arrows depicting flow behaviour in a cell for six different oscillation phases. a)  $\Phi = 3\pi/2$  b)  $\Phi = 11\pi/10$  c)  $\Phi = \pi/5$  d)  $\Phi = 9\pi/20$  e)  $\Phi = 7\pi/4$  f)  $\Phi = 48\pi/25$

To explore further the influence of baffle offsetting, simulations were carried out for  $a/L=0.15$  and  $a/L=0.5$  whilst keeping the rest of the parameters the same as for the simulations shown in Figure 15. A series of parameters were evaluated to quantitatively compare these three geometries. The first two, instantaneous axial and transverse absolute averaged velocities, are defined as

$$U(t) = \frac{1}{A_{unit\ cell}} \iint |u(t)| dA \quad (9)$$

$$V(t) = \frac{1}{A_{unit\ cell}} \iint |v(t)| dA \quad (10)$$

respectively. They are the integrated absolute values of the axial and radial velocities in a reactor's cell, divided by its area. From these values, the velocity ratio can also be easily calculated as

$$R_v(t) = U(t)/V(t) \quad (11)$$

Of course, these quantities are time-dependent, so their mean and maximum values for an oscillation cycle were computed, and results presented in Table 4.

Table 4 Mean and maximum values for U, V and  $1/R_v$

<b>a/L</b>		<b>U</b>	<b>V</b>	<b><math>1/R_v</math></b>
<b>0.15</b>	Mean	$2.147 \times 10^{-2}$	$0.897 \times 10^{-2}$	0.462
	Maximum	$3.415 \times 10^{-2}$	$1.099 \times 10^{-2}$	0.720
<b>0.3794</b>	Mean	$1.989 \times 10^{-2}$	$0.921 \times 10^{-2}$	0.513
	Maximum	$3.306 \times 10^{-2}$	$1.162 \times 10^{-2}$	0.935
<b>0.5</b>	Mean	$1.965 \times 10^{-2}$	$0.920 \times 10^{-2}$	0.523
	Maximum	$3.299 \times 10^{-2}$	$1.171 \times 10^{-2}$	0.983

From the results in Table 4, it can be observed how the values correlate to the simulation results. The optimum geometry for  $\eta$  maximises  $V_{\text{mean}}$ , and hence it achieves the maximum transversal mobility of the particles. However, this does not make this particular geometry the best in terms of RTD, since U (which is correlated to axial dispersion) has not been minimised. The lowest value of U is achieved for  $a/L=0.5$ , geometry which also maximises  $1/R_v$  and that is proven to have the narrowest RTD for these configurations.

## 6. Conclusions

This paper proposes the first multi-objective optimisation strategy for COBRs and in particular addresses a novel design of miniature COBR suitable for use in the early stages of chemical process development. Results presented here show the importance of the developed methodology where the temporal and spatial periodic flow field is analysed in order to identify the times and locations at which representative flow field data can be retrieved from CFD simulations. Performance-based metrics based on mixing efficiency index and the standard deviation of the residence time distribution are proposed and it is shown that Machine Learning during the cross-validation stage is crucial in obtaining an optimal calibration between the training and test datasets.

The surrogate models provide valuable insight into the influence of key design variables. In the case of the mixing efficiency, the parameters  $e/D$  and  $a/L$  have the biggest effect on the performance, achieving the maximum  $\eta$  values when  $e/D \approx 0.34$  and  $a/L \approx 0.38$ , regardless of  $L/D$ . This novel offset baffle configuration is proven to maximise the transversal mobility of the particles through inducing asymmetries in the flow. The residence time distribution tends to be narrower for higher values of  $L/D$ . This is rationally explained as the smaller width of the cells reduces the contact area between axially adjacent volumes of fluid. The parameter  $a/L$  reveals itself as crucial with  $a/L = 0.5$  giving the narrowest RTD. Under these conditions, the resulting design is akin to a reactor with twice as many cells created by baffles on alternate sides of the flow channel as compared to the  $a/L=0$  case where a pair of opposing baffles creates only a single cell.

These surrogate models can be used within a multi-objective optimisation process to create Pareto fronts from which design decisions can be made, exploiting the trade-off between the competing objectives. Our proposed configuration (point b in Figure 14) increases  $\eta$  at relatively little cost for  $\sigma^2$ , and outperforms any configuration that does not include baffle offsetting for both conflicting objectives. The methodology introduced here can be extended to incorporate additional design variables and three-dimensional flow analyses, in which the challenge will be to constrain the additional computational costs within feasible timescales. It could also be used to optimise a wide range of other chemical reactor systems either for process development or in actual manufacture.

Finally, the work highlights how the vortex development induced by the inclusion of baffle offsetting is different from the standard COBR design much explored within the literature and where there is no baffle offset within the design.

## 7. References

- [1] R. L. Hartman, J. P. McMullen, and K. F. Jensen, "Deciding Whether To Go with the Flow: Evaluating the Merits of Flow Reactors for Synthesis," *Angewandte Chemie-International Edition*, vol. 50, pp. 7502-7519, 2011.
- [2] T. Bergander, K. Nilsson-Välímää, K. Öberg, and K. M. Lacki, "High-Throughput Process Development: Determination of Dynamic Binding Capacity Using Microtiter Filter Plates Filled with Chromatography Resin," *Biotechnology Progress*, vol. 24, pp. 632-639, 2008.
- [3] C. Simms and J. Singh, "Rapid Process Development and Scale-Up Using A Multiple Reactor System," *Organic Process Research & Development*, vol. 4, pp. 554-562, 2000.
- [4] J. R. McDonough, A. N. Phan, and A. P. Harvey, "Rapid process development using oscillatory baffled mesoreactors – A state-of-the-art review," *Chemical Engineering Journal*, vol. 265, pp. 110-121, 2015.
- [5] R. Porta, M. Benaglia, and A. Puglisi, "Flow Chemistry: Recent Developments in the Synthesis of Pharmaceutical Products," *Organic Process Research & Development*, vol. 20, pp. 2-25, 2016.
- [6] S. V. Ley, "On Being Green: Can Flow Chemistry Help?," *The Chemical Record*, vol. 12, pp. 378-390, 2012.
- [7] N. Holmes, G. R. Akien, A. J. Blacker, R. L. Woodward, R. E. Meadows, and R. A. Bourne, "Self-optimisation of the final stage in the synthesis of EGFR kinase inhibitor AZD9291 using an automated flow reactor," *Reaction Chemistry & Engineering*, vol. 1, pp. 366-371, 2016.
- [8] M. Rueping, T. Bootwicha, and E. Sugiono, "Continuous-flow catalytic asymmetric hydrogenations: Reaction optimization using FTIR inline analysis," *Beilstein Journal of Organic Chemistry*, vol. 8, pp. 300-307, 2012.
- [9] M. C. Mitchell, V. Spikmans, and A. J. d. Mello, "Microchip-based synthesis and analysis: Control of multicomponent reaction products and intermediates," *Analyst*, vol. 126, pp. 24-27, 2001.
- [10] X. Yao, Y. Zhang, L. Du, J. Liu, and J. Yao, "Review of the applications of microreactors," *Renewable and Sustainable Energy Reviews*, vol. 47, pp. 519-539, 2015.

- [11] J. S. Moore and K. F. Jensen, "“Batch” Kinetics in Flow: Online IR Analysis and Continuous Control," *Angewandte Chemie International Edition*, vol. 53, pp. 470-473, 2014.
- [12] K. S. Elvira, X. C. I. Solvas, R. C. R. Wootton, and A. J. deMello, "The past, present and potential for microfluidic reactor technology in chemical synthesis," *Nature Chemistry*, vol. 5, pp. 905-915, 2013.
- [13] J. S. Moore and K. F. Jensen, "Automated Multitrajectory Method for Reaction Optimization in a Microfluidic System using Online IR Analysis," *Organic Process Research & Development*, vol. 16, pp. 1409-1415, 2012.
- [14] V. Sans and L. Cronin, "Towards dial-a-molecule by integrating continuous flow, analytics and self-optimisation," *Chemical Society Reviews*, vol. 45, pp. 2032-2043, 2016.
- [15] N. Holmes, G. R. Akien, R. J. D. Savage, C. Stanetty, I. R. Baxendale, A. J. Blacker, et al., "Online quantitative mass spectrometry for the rapid adaptive optimisation of automated flow reactors," *Reaction Chemistry & Engineering*, vol. 1, pp. 96-100, 2016.
- [16] M. I. Jeraal, N. Holmes, G. R. Akien, and R. A. Bourne, "Enhanced process development using automated continuous reactors by self-optimisation algorithms and statistical empirical modelling," *Tetrahedron*, vol. 74, pp. 3158-3164, 2018.
- [17] T. Wirth, *Microreactors in organic synthesis and catalysis*, 2 ed. Weinheim; Chichester: Wiley-VCH ; John Wiley [distributor], 2013.
- [18] E. L. Paul, V. A. Atiemo-Obeng, and S. M. Kresta, *Handbook of industrial mixing science and practice*, 18 ed. Hoboken, N.J: Wiley-Interscience, 2004.
- [19] O. Levenspiel, *Chemical reaction engineering*, 3 ed. New York: John Wiley & Sons, 1999.
- [20] H. Wang, A. Mustaffar, A. N. Phan, V. Zivkovic, D. Reay, R. Law, et al., "A review of process intensification applied to solids handling," *Chemical Engineering and Processing: Process Intensification*, vol. 118, pp. 78-107, 2017.
- [21] T. McGlone, N. E. B. Briggs, C. A. Clark, C. J. Brown, J. Sefcik, and A. J. Florence, "Oscillatory Flow Reactors (OFRs) for Continuous Manufacturing and Crystallization," *Organic Process Research & Development*, vol. 19, pp. 1186-1202, 2015.
- [22] A. W. Fitch, H. Jian, and X. Ni, "An investigation of the effect of viscosity on mixing in an oscillatory baffled column using digital particle image velocimetry and computational fluid dynamics simulation," *Chemical Engineering Journal*, vol. 112, pp. 197-210, 2005.
- [23] M. S. R. Abbott, A. P. Harvey, G. V. Perez, and M. K. Theodorou, "Biological processing in oscillatory baffled reactors: operation, advantages and potential," *Interface focus*, vol. 3, p. 20120036, 2013.
- [24] A. P. Harvey, M. R. Mackley, and T. Seliger, "Process intensification of biodiesel production using a continuous oscillatory flow reactor," *Journal of Chemical Technology & Biotechnology*, vol. 78, pp. 338-341, 2003.
- [25] E. Lobry, T. Lasuye, C. Gourdon, and C. Xuereb, "Liquid–liquid dispersion in a continuous oscillatory baffled reactor – Application to suspension polymerization," *Chemical Engineering Journal*, vol. 259, pp. 505-518, 2015.
- [26] S. Lawton, G. Steele, P. Shering, L. Zhao, I. Laird, and X.-W. Ni, "Continuous Crystallization of Pharmaceuticals Using a Continuous Oscillatory Baffled Crystallizer," *Organic Process Research & Development*, vol. 13, pp. 1357-1363, 2009.
- [27] M. R. Mackley, K. B. Smith, and N. P. Wise, "Mixing and separation of particle suspensions using oscillatory flow in baffled tubes," *Chemical Engineering Research and Design*, vol. 71, pp. 649-656, 1993.

- [28] A. Mazubert, J. Aubin, S. Elgue, and M. Poux, "Intensification of waste cooking oil transformation by transesterification and esterification reactions in oscillatory baffled and microstructured reactors for biodiesel production," *Green Processing and Synthesis*, vol. 3, pp. 419-429, 2014.
- [29] M. Palma and R. Giudici, "Analysis of axial dispersion in an oscillatory-flow continuous reactor," *Chemical Engineering Journal*, vol. 94, pp. 189-198, 2003.
- [30] M. R. Chapman, M. H. T. Kwan, G. King, K. E. Jolley, M. Hussain, S. Hussain, et al., "Simple and Versatile Laboratory Scale CSTR for Multiphasic Continuous-Flow Chemistry and Long Residence Times," *Organic Process Research & Development*, vol. 21, pp. 1294-1301, 2017.
- [31] H. S. Fogler, *Elements of chemical reaction engineering*, 5 ed. Boston: Prentice Hall, 2016.
- [32] A. P. Harvey, M. R. Mackley, and P. Stonestreet, "Operation and Optimization of an Oscillatory Flow Continuous Reactor," *Industrial & Engineering Chemistry Research*, vol. 40, pp. 5371-5377, 2001.
- [33] N. Reis, A. A. Vicente, J. A. Teixeira, and M. R. Mackley, "Residence times and mixing of a novel continuous oscillatory flow screening reactor," *Chemical Engineering Science*, vol. 59, pp. 4967-4974, 2004.
- [34] A. N. Phan and A. Harvey, "Development and evaluation of novel designs of continuous mesoscale oscillatory baffled reactors," *Chemical Engineering Journal*, vol. 159, pp. 212-219, 2010.
- [35] A. N. Phan, A. Harvey, and J. Lavender, "Characterisation of fluid mixing in novel designs of mesoscale oscillatory baffled reactors operating at low flow rates (0.3–0.6ml/min)," *Chemical Engineering and Processing: Process Intensification*, vol. 50, pp. 254-263, 2011.
- [36] A. N. Phan and A. P. Harvey, "Effect of geometrical parameters on fluid mixing in novel mesoscale oscillatory helical baffled designs," *Chemical Engineering Journal*, vol. 169, pp. 339-347, 2011.
- [37] O. Okafor, A. Weilhard, J. A. Fernandes, E. Karjalainen, R. Goodridge, and V. Sans, "Advanced reactor engineering with 3D printing for the continuous-flow synthesis of silver nanoparticles," *Reaction Chemistry & Engineering*, vol. 2, pp. 129-136, 2017.
- [38] F. Almeida, F. Rocha, and A. Ferreira, "Analysis of Liquid Flow and Mixing in an Oscillatory Flow Reactor Provided with 2D Smooth Periodic Constrictions," *U.Porto Journal of Engineering*, vol. 4, pp. 1-15, 2018.
- [39] M. Mikko, G. Elena, I. Kirsi, and N. Xiong-Wei, "Evaluation of axial dispersion and mixing performance in oscillatory baffled reactors using CFD," *Journal of Chemical Technology & Biotechnology*, vol. 88, pp. 553-562, 2013.
- [40] A. Mazubert, D. F. Fletcher, M. Poux, and J. Aubin, "Hydrodynamics and mixing in continuous oscillatory flow reactors—Part I: Effect of baffle geometry," *Chemical Engineering and Processing: Process Intensification*, vol. 108, pp. 78-92, 2016.
- [41] A. Mazubert, D. F. Fletcher, M. Poux, and J. Aubin, "Hydrodynamics and mixing in continuous oscillatory flow reactors—Part II: Characterisation methods," *Chemical Engineering and Processing: Process Intensification*, vol. 102, pp. 102-116, 2016.
- [42] N. Reis, A. P. Harvey, M. R. Mackley, A. A. Vicente, and J. A. Teixeira, "Fluid Mechanics and Design Aspects of a Novel Oscillatory Flow Screening Mesoreactor," *Chemical Engineering Research and Design*, vol. 83, pp. 357-371, 2005.
- [43] X. Ni, M. R. Mackley, A. P. Harvey, P. Stonestreet, M. H. I. Baird, and N. V. R. Rao, "Mixing through oscillations and pulsations - A guide to achieving process enhancements in the chemical and process industries," *Chemical Engineering Research & Design*, vol. 81, pp. 373-383, 2003.

- [44] X. Ni, G. Brogan, A. Struthers, D. C. Bennett, and S. F. Wilson, "A Systematic Study of the Effect of Geometrical Parameters on Mixing Time in Oscillatory Baffled Columns," *Chemical Engineering Research and Design*, vol. 76, pp. 635-642, 1998.
- [45] B. Finlayson, A. Aditya, V. Brasher, L. Dahl, H. Quan Dinh, A. Field, et al., "Mixing of Liquids in Microfluidic Devices," presented at the COMSOL Conference, Boston, USA, 2008.
- [46] E. L. Cussler, *Diffusion: Mass Transfer in Fluid Systems*, 3 ed. Cambridge: Cambridge University Press, 2009.
- [47] B. Armaly, Durst, F., Pereira, J., & Schönung, B., "Experimental and theoretical investigation of backward-facing step flow," *Journal of Fluid Mechanics*, vol. 127, pp. 473-496, 1983.
- [48] P. Sung-Jin, K. Jung Kyung, P. Junha, C. Seok, C. Chanil, and C. Jun Keun, "Rapid three-dimensional passive rotation micromixer using the breakup process," *Journal of Micromechanics and Microengineering*, vol. 14, p. 6, 2004.
- [49] A. D. Stroock, S. K. W. Dertinger, A. Ajdari, I. Mezić, H. A. Stone, and G. M. Whitesides, "Chaotic Mixer for Microchannels," *Science*, vol. 295, pp. 647-651, 2002.
- [50] R. H. Liu, M. A. Stremler, K. V. Sharp, M. G. Olsen, J. G. Santiago, R. J. Adrian, et al., "Passive mixing in a three-dimensional serpentine microchannel," *Journal of Microelectromechanical Systems*, vol. 9, pp. 190-197, 2000.
- [51] B. Stoeber, D. Liepmann, and S. J. Muller, "Strategy for active mixing in microdevices," *Physical Review E*, vol. 75, p. 066314, 2007.
- [52] Y. Li, R. K. Reddy, C. S. S. R. Kumar, and K. Nandakumar, "Computational investigations of the mixing performance inside liquid slugs generated by a microfluidic T-junction," *Biomicrofluidics*, vol. 8, p. 054125, 2014.
- [53] A. Hashmi and J. Xu, "On the Quantification of Mixing in Microfluidics," *Journal of Laboratory Automation*, vol. 19, pp. 488-491, 2014.
- [54] R. T. Haftka, D. Villanueva, and A. Chaudhuri, "Parallel surrogate-assisted global optimization with expensive functions – a survey," *Structural and Multidisciplinary Optimization*, vol. 54, pp. 3-13, 2016.
- [55] K. Choi, B. D. Youn, and R.-J. Yang, *Moving least square method for reliability-based design optimization*, 2001.
- [56] E. Loweth, G. de Boer, and V. Toropov, "Practical recommendations on the use of moving least squares metamodel building," in *13th International Conference on Civil, Structural and Environmental Engineering Computing*, Crete, Greece, 2011.
- [57] Q.-S. Xu and Y.-Z. Liang, "Monte Carlo cross validation," *Chemometrics and Intelligent Laboratory Systems*, vol. 56, pp. 1-11, 2001.
- [58] R. Kohavi, "A study of cross-validation and bootstrap for accuracy estimation and model selection," presented at the *Proceedings of the 14th international joint conference on Artificial intelligence - Volume 2*, Montreal, Quebec, Canada, 1995.
- [59] R. R. Picard and R. D. Cook, "Cross-Validation of Regression Models," *Journal of the American Statistical Association*, vol. 79, pp. 575-583, 1984.
- [60] "Bias Variance Decomposition," in *Encyclopedia of Machine Learning*, C. Sammut and G. I. Webb, Eds., ed Boston, MA: Springer US, 2010, pp. 100-101.

